

A theoretical explanation of grain size distributions in explosive rock fragmentation

A. C. Fowler^{1,2} and Bettina Scheu³

¹MACSI, University of Limerick, Limerick, Ireland

²OCIAM, University of Oxford, Oxford, UK

³Earth and Environmental Sciences, LMU München, München, Germany

May 5, 2016

Abstract

We have measured grain size distributions of the results of laboratory decompression explosions of volcanic rock. The resulting distributions can be approximately represented by gamma distributions of weight per cent as a function of $\phi = -\log_2 d$, where d is grain size in millimetres measured by sieving, with a superimposed long tail associated with the production of fines. We provide a description of the observations based on sequential fragmentation theory, which we develop for the particular case of ‘self-similar’ fragmentation kernels, and we show that the corresponding evolution equation for the distribution can be explicitly solved, yielding the long time lognormal distribution associated with Kolmogorov’s fragmentation theory. Particular features of the experimental data, notably time evolution, advection, truncation and fines production, are described and predicted within the constraints of a generalised, ‘reductive’ fragmentation model, and it is shown that the gamma distribution of coarse particles is a natural consequence of an assumed uniform fragmentation kernel. We further show that that an explicit model for fines production during fracturing can lead to a second gamma distribution, and that the sum of the two provides a good fit to the observed data.

Keywords: Rock fragmentation, grain size distribution, sequential fragmentation theory.

1 Introduction

Fragmentation is a ubiquitous phenomenon in many natural and engineering systems. It is the process by which an initially competent medium, whether solid or

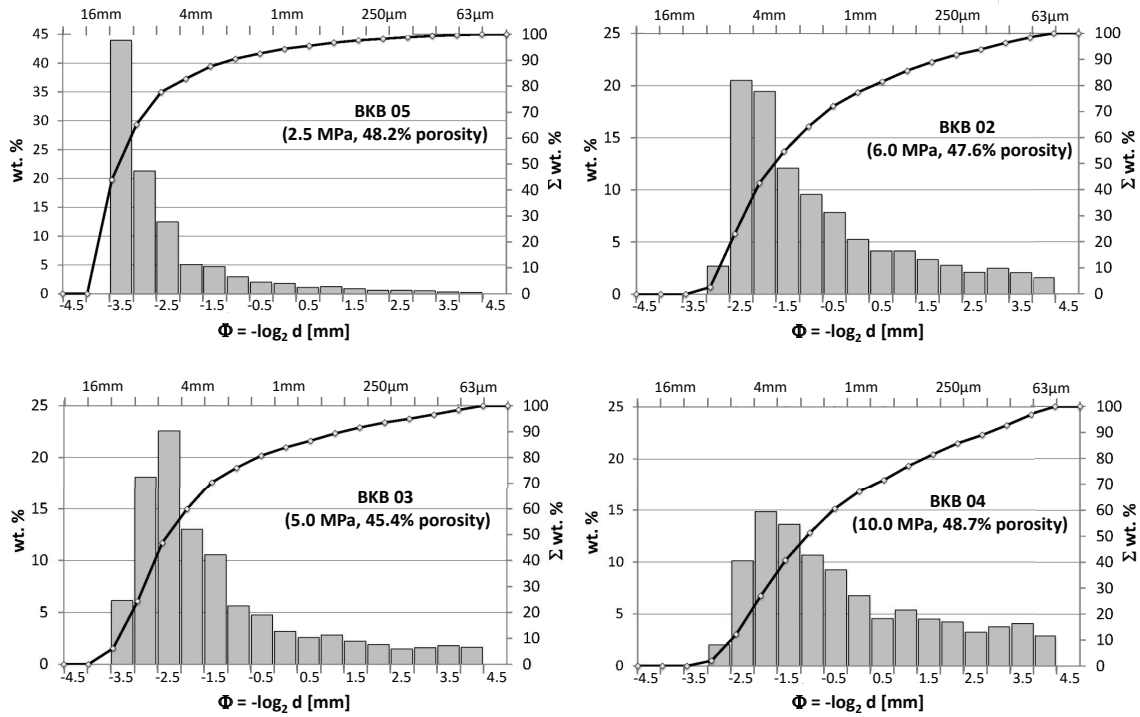


Figure 1: Bar charts of four breadcrustbomb (BKB) samples, a volcanic rock from Unzen volcano, Japan, exposed to rapid decompression from different applied pressure to atmospheric conditions. All samples used for this study have a very similar connected porosity. All experiments are conducted at ambient temperature, following the same experimental procedure.

liquid, is broken up into a population of constituents. Examples occur in collisions and impacts of asteroids/meteorites, explosion driven fragmentation of munitions on a battlefield, as well as of magma in a volcanic conduit causing explosive volcanic eruptions, rock explosions in mining, break-up of liquid drops, and many industrial processes, such as atomization and spraying (Turcotte 1986, Brown 1989, Villiermaux 2007, Elek and Jaramaz 2008). Besides the mechanism of fragmentation the resulting frequency-size distribution of the generated constituents is of central interest. Initially their distributions were fitted empirically using lognormal, Rosin-Rammler and Weibull distributions (Brown and Wohletz 1995 and references therein). The sequential fragmentation theory (Brown 1989, Wohletz *et al.* 1989, Wohletz and Brown 1995, Mackaman-Loffland *et al.* 2014) and the application of fractal theory to fragmentation products (Turcotte 1986, Perfect 1997, Rieu and Perrier 1998, Perugini and Kueppers 2012) attempt to circumvent this empiricism by providing a more physical basis for the applied distribution. Both rely on an at least partially scale-invariant and thus self-similar random fragmentation process.

Our present interest stems from the mechanism by which explosive volcanic eruptions occur, and in particular from experiments in which vesicular volcanic rock sam-

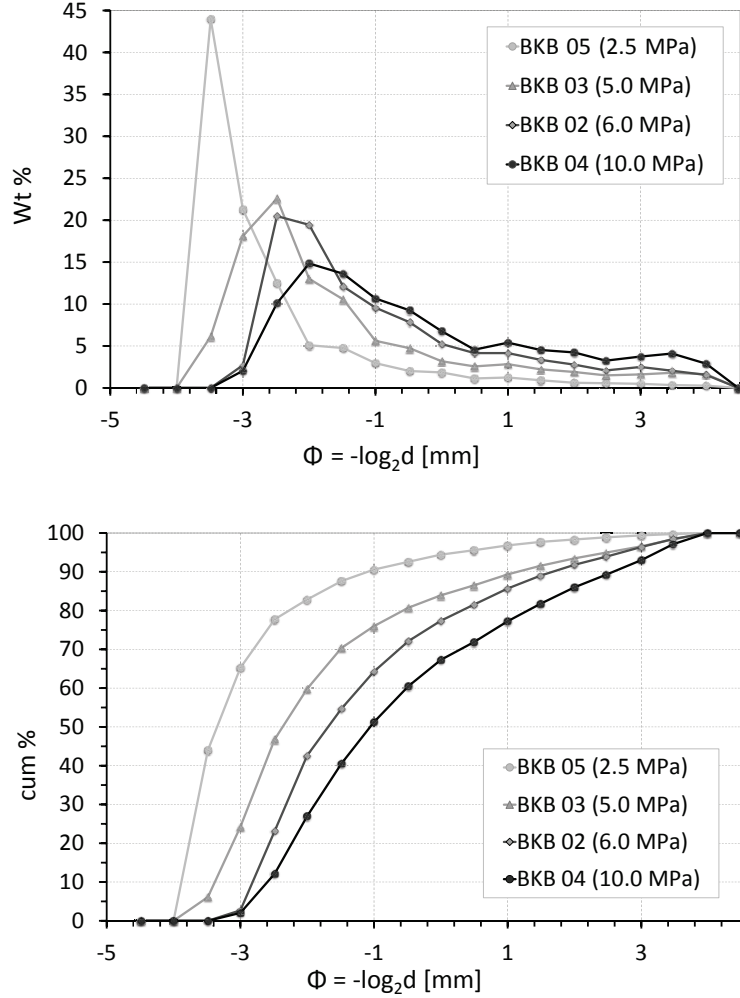


Figure 2: Grain size distribution (GSD) of the same samples from Unzen volcano as in figure 1, but now plotted as differential weight fraction of particles (top), and as cumulative weight fraction of particles (bottom) against sieve size ϕ (ϕ is defined in (2.1)). Each point represents the middle of a bin. All experiments are performed at ambient temperature with as similar as possible rock samples. Increasing darkness of curves indicates increasing applied pressure.

ples explode naturally when suddenly depressurised from initial pressures of tens of MPa to ambient conditions (Scheu *et al.* 2006, 2008). The physics governing this fragmentation process has been successfully modelled and the observed fragmentation pattern can be numerically reproduced (Fowler *et al.* 2010). In these experiments, the fragmentation of natural rocks leads to grain size distributions which vary depending on the experimental starting conditions; typical examples of these are shown in figures 1 and 2. While our earlier theory provided an explanation for the fragmentation patterns observed, it did not consider the grain size distribution.

Our purpose in this paper is to provide a stochastic model for the evolution of the grain size distribution during the explosion process, and thus to provide a theoretical description of the different distributions which are shown in figures 1 and 2. Our model combines a sequential model of the type outlined by Turcotte (1986), but generalised to cater for the explosive process appropriate here, in particular by including in the description of the fracturing events in which the rock fragments a recipe for the production of fines, as observed in the experiments.

2 Experimental products and theory of explosive magma fragmentation

Constraining dynamics and products of explosive fragmentation of vesicular magma and rocks is key to better understanding volcanic eruptions and their associated products. Laboratory experiments have been conducted for almost 20 years with increasing vigour, investigating various aspects of fragmentation behaviour of magma analogues (e.g., Mader *et al.* 1994, Phillips *et al.* 1995, Ichihara *et al.* 2002, Namiki and Manga 2008) as well as natural rocks and magmas (e.g., Alidibirov and Dingwell 1996, Spieler *et al.* 2003, Spieler *et al.* 2004, Kueppers *et al.* 2006, Scheu *et al.* 2006, 2008, Mueller *et al.* 2008, Kremers *et al.* 2010, Alatorre-Ibargüengoitia *et al.* 2011, Perugini *et al.* 2012, Richard *et al.* 2013, Rager *et al.* 2014). Experiments on rocks and magmas are conducted in a shock-tube apparatus where samples are exposed to rapid decompression from various starting conditions in the form of applied pressures ranging from 2 to 40 MPa and temperatures between 20 to 900° C. This study uses experiments at ambient temperature only, however very similar grain size distributions are also found for high temperature experiments (Spieler *et al.* 2003, Kueppers *et al.* 2006) owing to the brittle nature of these very fast processes.

Starting conditions are reached by slow gradual build up of temperature and gas pressure using either argon or nitrogen gas; a dwell period prior to rapid decompression assures equilibrium conditions and negligible path effects. Rapid decompression is triggered by the bursting of a series of diaphragms, separating the high-pressure section with the sample from a large low pressure section, into which the generated clasts will be ejected. The low-pressure section is tailored to an efficient collection of the clasts, reducing the loss of very fine clasts to a minimum.

In this study we analyse the products obtained from rapid decompression experiments of a breadcrustbomb (BKB), a volcanic rock from Unzen Volcano, Japan. Cylindrical samples (diameter: 24 mm, length: 50-60 mm) were drilled out of a larger block. The connected porosity of each sample was determined from its geometrical volume and the matrix volume obtained by helium pycnometry. All samples exhibit very similar values of connected porosity between 45% – 49%. Isolated porosity was always estimated to be in the order of a few percent only; thus a significant role of isolated porosity on the evolution of grain size distribution can be ruled out. The experiments were conducted at ambient temperature in a transparent autoclave and monitored with a high-speed video camera. Applied pressure was varied between

2.5 and 10 MPa, higher pressures were inhibited by the autoclave’s strength. Figure 1 shows the individual grain size distributions of the clasts generated at increasing applied pressures. Size distributions were obtained by manual dry sieving at half- ϕ steps (Cas and Wright 1987 pp. 476–478, and references therein), where

$$\phi = -\log_2(d/d_1), \quad (2.1)$$

d is the particle diameter and $d_1 = 1$ mm; thus the equation above is often written as $\phi = -\log_2 d$. The natural upper limit of the grain size distribution is given by the sample itself fitting through a sieve mesh, thus $\phi = -5$ (equivalent to 32 mm) is assumed to be the coarsest fraction. The finest grain fraction used in this study corresponds to $\phi = 4$ (equivalent to $63 \mu\text{m}$). Figure 2 comprises all four data sets as differential weight fraction of particles (top) or as cumulative weight fraction of particles (bottom), both plotted against ϕ . In both, the change of the distribution in shape as well as in position with increasing applied pressure can be seen. Further grain size distributions derived from rapid decompression experiments on volcanic rocks can be found for instance in Spieler *et al.* (2003) and Kueppers *et al.* (2006). These distributions are very similar to the BKB ones in shape, as well as in their responses to changes in the applied pressure. Such differences as do occur are mainly attributed to different samples being used, i. e., different connected porosity and permeability. Thus we consider the grain size distributions presented in Figures 1 and 2 to be representative for rapid decompression-induced fragmentation of vesicular rocks at increasing applied pressure. The advantage of the data set presented here lies both in its cleanness, and in the additional monitoring of the fragmentation process which was obtained using a high-speed camera. This allowed further analysis of the individual fragmentation events which occurred in each sample.

The experimentally generated grain size distributions do not reflect any transport-related sorting, and in that they differ from the grain size distribution of natural volcanic deposits. Their closest natural counterparts are the total grain size distributions (TGSD), which are harder to obtain, but more relevant to eruption dynamics (Bonadonna and Houghton 2005, Girault 2014). We neglect transport-related grain size changes due to abrasion, collisions (particle-particle and particle-tank) and comminution, as these secondary effects scale with the fragmentation depth (Dufek *et al.* 2012), i. e., the length of the experimental conduit, which is rather short in our laboratory setting (~ 25 cm). However these secondary grain size reductions also depend on (i) initial size distribution and (ii) fragmentation dynamics, as the ejected clasts and surrounding gas do not form a continuous granular flow with homogeneous density distribution, but a heterogeneous granular flow with variable density. The shape of the grain size distribution depends on the fragmentation process; for the data set analysed here it depends in particular on the applied pressure: the higher the pressure, the more fragmentation events will occur before the pressure is reduced. In case of an applied pressure just slightly above the pressure needed to fragment the sample, only a few fragmentation events will occur, and a longer time lies between these events.

3 Sequential fragmentation theory

The basic mechanism of the theory of fragmentation was described by Kolmogorov (1941). He explained how a lognormal distribution of grain sizes could arise through the successive fragmentation of a rock sample. If the splitting position occurs at random, then the successive segments have diameters d_i given by $d_{i+1} = f_i d_i$, where f_i is drawn from a random distribution on $(0, 1)$. Thus

$$\ln d_{i+1} = \ln d_i + \ln f_i; \quad (3.1)$$

the increments of $\ln d_i$ are random, and thus the central limit theorem implies that for large n , $\ln d_n$ is normally distributed, i. e., d_n is lognormally distributed.

Brown (1989) and Wohletz *et al.* (1989) introduce a theory called sequential fragmentation theory, which they use to explain observed distributions in various rock fragment populations. Their theory is discussed further below. Its context is that of a stochastic process, in which the continuous time evolution of the grain size distribution $n(x, t)$, where n is number density and x is fragment volume (specifically, $n(x, t) dx$ is the number of fragments having volume in the range $(x, x + dx)$), can be written in terms of a master equation which takes the form (Kaminski and Jaupart 1998, Cheng and Redner 1990)

$$\frac{\partial n}{\partial t} = \int_x^\infty p(y) K(x, y) n(y, t) dy - p(x) n, \quad (3.2)$$

where $p(x)$ is the probability (per unit time) of fragmenting rocks of size x at time t , and $K(x, y)$ is the fragmentation distribution of particles of size x from fragmentation of a rock of size y . Note that the time scale of the problem is just p^{-1} . If x_0 is the volume of the initial block, then

$$\int_0^\infty x n dx = x_0, \quad (3.3)$$

and is conserved. Evidently we must have $x < y$, so that

$$K(x, y) = 0, \quad x > y, \quad (3.4)$$

so that the lower limit in the integral in (3.2) can be taken to be zero; additionally, volume conservation during fragmentation requires

$$\int_0^y x K(x, y) dx = y. \quad (3.5)$$

Much of the literature on fragmentation revolves around measurements of distributions having a power law distribution in part of the range, and this is commonly thought to imply a self-similar process (Turcotte 1997). Two examples which we will focus on are Turcotte's own, where a cubic block is fractured into eight sub-blocks of equal size (Turcotte 1986), and Brown and Wohletz's (1995) power law kernel,

designed to produce a commonly assumed Weibull distribution, and popular amongst volcanologists (e.g., Mackaman-Lofland *et al.* 2014).

Turcotte's model defines a kernel K in terms of a delta function (essentially a point source),

$$K(x, y) = \frac{1}{\lambda} \delta(x - \lambda y), \quad (3.6)$$

where $\lambda < 1$ is the volume fraction of the blocks which result from the fracturing event; in Turcotte's model $\lambda = \frac{1}{8}$. By contrast, Brown and Wohletz's (1995) model (which we will call the Brown model) takes $K = Cx^{\nu-1}$ (in Brown and Wohletz (1995), $\nu = 1 + \gamma \in (0, 1)$). Brown and Wohletz take C to be constant, but this is inconsistent with the requirement in (3.5), and the correct form for K is

$$K(x, y) = \frac{1 + \nu}{y} \left(\frac{x}{y} \right)^{\nu-1}, \quad (3.7)$$

which satisfies (3.5). Later we will focus on the Brown kernel, which is suitable for our needs, but first we provide a new and general theory for a class of such self-similar kernels.

3.1 Self-similar fragmentation

The purpose of this section is to show that for *self-similar fragmentation*, the integral in (3.2) takes a particularly simple form, of convolution type. We define a general self-similar kernel to be one of the form

$$K(x, y) = \frac{1}{y} g\left(\frac{x}{y}\right), \quad \int_0^\infty \eta g(\eta) d\eta = 1, \quad g = 0 \quad \text{for} \quad \eta > 1; \quad (3.8)$$

the Turcotte (T) and Brown (B) kernels are then of the form

$$g(\eta) = \begin{cases} \frac{1}{\lambda} \delta(\eta - \lambda), & \text{(T),} \\ (1 + \nu) \eta^{\nu-1}, & \text{(B),} \end{cases} \quad (3.9)$$

We can also define a generalised Turcotte model (GT) which splits a block up into a number of different-sized fragments, of fractions $\lambda_1, \lambda_2, \dots$ of the original block size. The resulting GT kernel is

$$g(\eta) = \sum_i \delta(\eta - \lambda_i), \quad \sum_i \lambda_i = 1. \quad (3.10)$$

The Turcotte model is reclaimed by choosing $\lambda_1 = \dots = \lambda_8 = \frac{1}{8}$.

It is convenient to relate particle size x to the sieve size variable ϕ introduced in (2.1); the two are related by

$$x = x_1 \exp(-A\phi), \quad x_1 = \frac{1}{6} \pi d_1^3, \quad (3.11)$$

and $d_1 = 1$ mm as before. The value of A is

$$A = 3 \ln 2 = 2.08, \quad (3.12)$$

and is introduced to reduce the clutter associated with the definition of ϕ . Additionally, we relate the number density n to the volume or weight fraction density W measured in terms of ϕ , as shown in figure 2. Details of the calculations are given in the appendix. There we show that W satisfies the simplified equation

$$W_t = \int_{-\infty}^{\infty} G(s)W(\phi - s, t) ds - W, \quad (3.13)$$

where we have assumed that the fragmentation probability is uniform, $p = 1$ (note that this defines the time scale of the process). The kernel G is determined by g , and $G(s) = 0$ for $s < 0$, and additionally

$$\int_0^{\infty} G(\psi) d\psi = \int_0^{\infty} W(\psi, t) d\psi = 1. \quad (3.14)$$

The generalised Turcotte and Brown kernels take the form

$$G(\phi) = \begin{cases} \sum_i \lambda_i \delta\left(\phi - \frac{1}{A} \ln \frac{1}{\lambda_i}\right), & \sum_i \lambda_i = 1, \quad (\text{GT}), \\ (1 + \nu) A e^{-(1+\nu)A\phi}, & (\text{B}). \end{cases} \quad (3.15)$$

The initial condition for W is

$$W = \delta(\phi - \phi_0) \quad \text{at} \quad t = 0, \quad (3.16)$$

where

$$\phi_0 = -\frac{1}{A} \ln \left(\frac{x_0}{x_1} \right) \quad (3.17)$$

is the minimum value of ϕ . Since $W = 0$ for $\phi < \phi_0$, the upper limit of the integral in (3.13) can be equally be taken as $\phi - \phi_0$ (and the lower limit taken as 0, since $G = 0$ when $\psi < 0$).

As we mentioned earlier, Brown and Wohletz (1995) use their choice of kernel to motivate the derivation of the Weibull distribution. We also mentioned that their choice of kernel is inaccurate. Further, they derive the Weibull distribution by assuming the solution of (3.13) is a steady state one. This makes no sense. And in any case, no equilibrium solution of (3.13) exists unless $G(\phi) = \delta(\phi)$, in which case any distribution W is a solution.

The solution of (3.13) is easily found using the Fourier transform

$$\hat{W}(k, t) = \int_{-\infty}^{\infty} W(\phi, t) e^{ik\phi} d\phi, \quad (3.18)$$

and is given by

$$W(\phi, t) = w(\phi - \phi_0, t), \quad (3.19)$$

where the Fourier transform of w is

$$\hat{w} = \exp \left[t \left\{ \hat{G}(k) - 1 \right\} \right]; \quad (3.20)$$

in general the solution must be computed numerically.

Some useful insight can be obtained by solving the basic Turcotte model, for which we may take

$$G(s) = \delta(s - \alpha), \quad \alpha = \frac{1}{A} \ln a, \quad (3.21)$$

corresponding to division of each block into a equal sub-blocks; Turcotte took $a = 8$, but any integer will suffice, and in fact mathematically any positive number greater than one will do. (3.13) then reduces to

$$W_t = W(\phi - \alpha, t) - W, \quad W(\phi, 0) = \delta(\phi - \phi_0). \quad (3.22)$$

The solution consists of a sequence of varying amplitude delta functions at the points $\phi_0 + \alpha$, $\phi_0 + 2\alpha$, etc. and is determined by writing

$$u_r = \int_{(\phi_0 + r\alpha)_-}^{(\phi_0 + r\alpha)_+} W d\phi, \quad (3.23)$$

whence

$$\dot{u}_r = u_{r-1} - u_r, \quad (3.24)$$

with

$$u_0(0) = 1, \quad u_r(0) = 0, \quad r > 0. \quad (3.25)$$

The solution is the Poisson distribution

$$u_r = \frac{t^r e^{-t}}{r!}, \quad (3.26)$$

which fairly rapidly approaches a Gaussian. More complicated differential-difference equations can be created and solved using sequences $\lambda_1 = \lambda$, $\lambda_2 = \lambda^2$, etc. For example, this choice truncated at λ_2 yields a second order such equation, providing $\lambda = 0.618$ is the golden ratio. These problems are easily solved using generating functions, but useful closed form solutions equivalent to (3.26) are not easily come by.

The general solution w whose transform is given by (3.20) is

$$w = \frac{1}{2\pi} \int_{-\infty}^{\infty} \exp \left[t \left\{ \hat{G}(k) - 1 \right\} - ik\phi \right] dk, \quad (3.27)$$

and the large time solution is found by expanding the integrand for small k . Noting that $\hat{G}(0) = 1$, and the derivatives are

$$\hat{G}'(0) = iG_1, \quad \hat{G}''(0) = -G_2, \quad (3.28)$$

where

$$G_1 = \int_0^{\infty} xG(x) dx, \quad G_2 = \int_0^{\infty} x^2G(x) dx, \quad (3.29)$$



Figure 3: Evolution of the grain size distribution given by (3.27), where G corresponds to a uniform kernel $g(\eta) = 2$, $0 < \eta < 1$. Shown are the solutions at $t = 2, 4, 6, 8, 10$.

we have

$$w \approx \frac{1}{2\pi} \int_{-\infty}^{\infty} \exp \left[ik(G_1 t - \phi) - \frac{1}{2} G_2 t k^2 \dots \right] dk, \quad (3.30)$$

and calculating the integral, we find

$$w \sim \frac{1}{\sqrt{2\pi G_2 t}} \exp \left[-\frac{(\phi - G_1 t)^2}{2 G_2 t} \right], \quad (3.31)$$

which is a Gaussian whose mean propagates to the right (in ϕ) at speed G_1 . This is the manifestation of the central limit theorem, and since ϕ is the logarithm of particle size, it gives a lognormal distribution in particle size.

Figure 3 shows the evolution of w with time when G given by (A.3) corresponds to a choice of the fragmentation kernel g as a uniform function, $g = 2$, equivalent to the choice $\nu = 1$ in the Brown kernel (3.9). It can be seen that the solution approaches the Gaussian given by (3.31). A feature of note is that the value of w at $\phi = 0$ decreases exponentially with time, rather than descending instantly to zero. As we discuss in the following section, this is somewhat unrealistic in our experimental context. A further feature of note is that at large time the distribution decays faster than exponentially, unlike the fractal distribution (see the appendix) given by (A.7) (but note that for fixed time and large ϕ , the decay is weaker).

4 Application to rock fragmentation experiments

In considering the application of fragmentation theory to the experimental data, there are four issues to deal with, and we consider each of these in turn. These four issues are those of time evolution of the grain size distribution, the apparent self-similarity of the coarse fragment distribution, the apparent advection and truncation at coarse wavelengths of the distributions in figure 2, and the problem of the production of fines. Further, in order to account for some of these issues, we introduce what we call a reductive fragmentation theory.

4.1 Time evolution

One of the most striking features of the four graphs in the upper panel of figure 2 is the sense that they can be interpreted as a time evolution of a distribution, much as figure 3 shows a single evolving distribution; the distributions in figure 2 decay and move to the right as the initial confining pressure increases.

In order to understand why this should be so, we need to recall the mechanism of fragmentation, as discussed by Fowler *et al.* (2010). When a block fractures and separates from the column, its total stress $\sigma_{\text{tot}} = (1 - \phi)\sigma - \phi p$ rapidly relaxes to equal the external pressure in the chamber, p_c , which itself is rapidly decreasing with time. Here ϕ is the sample porosity, σ is the stress in the solid, and p is the pore pressure in the gas. It follows that the effective stress in the block is

$$\sigma_{\text{eff}} = \sigma_{\text{tot}} + p = (1 - \phi)(\sigma + p) \approx p - p_c, \quad (4.1)$$

and since the theoretical fracture criterion is $\sigma + p > \sigma_Y$, this criterion in the block is thus

$$p - p_c \gtrsim (1 - \phi)\sigma_Y. \quad (4.2)$$

The key feature of the experiments is that the chamber pressure relaxation time $t_c \approx 1$ ms is much smaller than the diffusive time scale $t_0 \approx 22$ ms for the gas pore pressure to relax due to exhalation from the block, and therefore, at least for large blocks, the time to the next fracture is essentially controlled by the time from the preceding fracture for the chamber pressure to decrease by the quantity $(1 - \phi)\sigma_Y$. Therefore, the higher the initial confining pressure, the longer does the fragmentation process continue, and thus the final GSD represents the evolution of the distribution to a longer time. It is because of this that experiments with different initial confining pressures yield results which can be interpreted as representing distribution evolution over different times. In the simplest interpretation, the initial confining overpressure would simply be proportional to the number of fracture events, but in reality the correspondence will not be linear, because the diffusive gas relaxation time decreases with the square of the block size, so that at some small scale, block fragmentation will cease. In summary, we interpret the GSDs from experiments at different initial confining pressures as representing proxy time sequences of a single evolving GSD, much in the same way as proxy time sequences of, for example, evolving plant root systems are studied from a population whose members are sacrificed at different times.

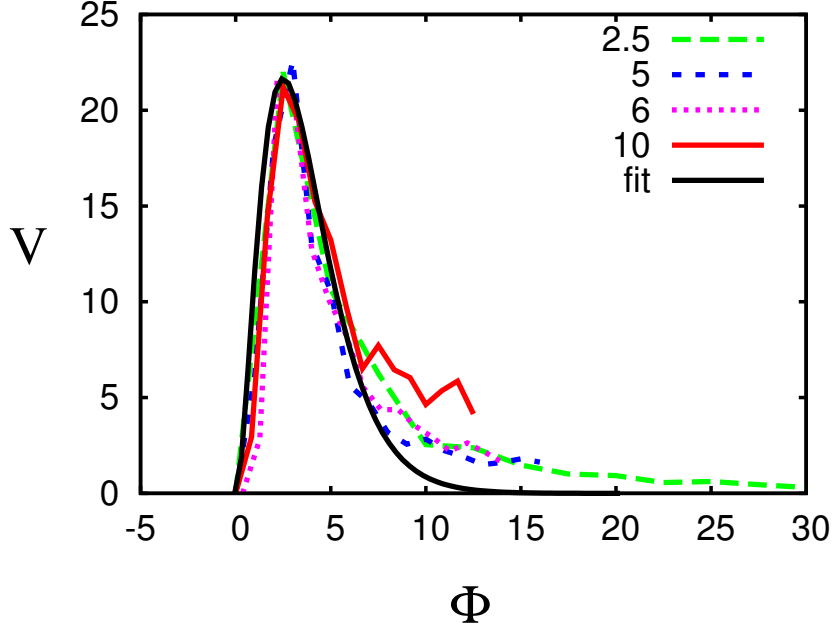


Figure 4: Collapse of the data $W(\phi, p_0)$ to an approximate single function $V(\Phi)$, and a fitting gamma distribution. The approximating functions are defined by $V = \frac{1}{2}W[0.2\Phi - 4, 2.5]$, $V = W[0.5\Phi - 4, 5]$, $V = \frac{1}{0.95}W[0.55\Phi - 3.7, 6]$, $V = \frac{1}{0.7}W[0.6\Phi - 3.5, 10]$, and the fitted curve is $\frac{100}{\Gamma(\nu)}\alpha^\nu\Phi^{\nu-1}e^{-\alpha\Phi}$, with $\alpha = 0.8$, $\nu = 3$.

4.2 Self-similarity

The self-similar nature of the long term solution (3.31) suggests we might seek a similar collapse of the experimental data on to a single curve, and figure 4 shows that such a collapse is possible, although the curves start to diverge at larger Φ ; the reasons for this are discussed below in subsection 4.5. Equally it is clear that the chosen fitting gamma distribution decays too rapidly at larger Φ , but while one could choose other curves to provide a better fit to the heavy tail, the later discussion indicates that there is no purpose to this.

4.3 Advection and truncation

Given that our fragmentation model has an explicit solution in (3.20) or (3.27), and that we can interpret the results of different initial confining pressures as representing different times in the evolution of the distribution, it is tempting to seek to fit the data in figure 2 by the choice of a suitable kernel G . Of course, the problem with this is that we have no real idea what to choose for G . We might try the various generalised Turcotte kernels, or the Brown kernels, but initial efforts in this direction all yield figures similar to figure 3. A more enterprising possibility is to use the data

to determine an approximate formula for w , and then use the inverse of (3.20), thus

$$\hat{G}(k) = 1 + \frac{1}{t} \ln \hat{w}, \quad (4.3)$$

to determine G . Efforts to do this fail, apparently because the inverse problem is ill-posed: (3.20) only has a solution for G if $\hat{w} \neq 0$, for example, although that in itself is not sufficient to provide a solution. For example, if we choose a gamma distribution as in figure 4,

$$w = \frac{1}{\Gamma(\nu)} \alpha^\nu \phi^{\nu-1} e^{-\alpha\phi}, \quad (4.4)$$

then

$$\hat{w} = \left(\frac{\alpha}{\alpha - ik} \right)^\nu, \quad (4.5)$$

and thus

$$\hat{G} = 1 + \frac{\nu}{t} \ln \left(\frac{\alpha}{\alpha - ik} \right). \quad (4.6)$$

But this cannot be the transform of an L^1 function G , as the Riemann-Lebesgue lemma implies that $\hat{G} \rightarrow 0$ as $k \rightarrow \infty$. Indeed, since $\hat{f}' = i\phi \hat{f}$ for any function f , the inverse transform of $\ln \left(\frac{\alpha}{\alpha - ik} \right)$ would have to be $f(\phi) = \frac{e^{-\alpha\phi}}{\phi}$, $\phi > 0$, $f(\phi) = 0$, $\phi < 0$, which is evidently nonsense.

The problem is that while there are some similarities in figure 3 to figures 1 and 2, there are some essential differences. Two which are critical are *truncation* and *advection*. Since the initial value of $\phi_0 \approx -5$, we see that in all samples, the value of W at $\phi = \phi_0$ goes to zero immediately; we call this truncation. Further, the first value of ϕ where $W = 0$ advances with time; we call this advection. Neither of these properties is satisfied by the solution of the master equation (3.13).

4.4 Reductive fragmentation theory

The physical reason for this is in fact obvious. After the initial fracture of the sample, it is split into two pieces, each of them smaller than the original. So long as the blocks continue to fracture, both truncation and advection will occur. In order to describe this, we revisit the derivation of the master equation. The equation (3.2) is derived from an incremental difference equation

$$n(x, t + \Delta t) = n(x, t)[1 - p(x)\Delta t] + \int_0^\infty p(y)\Delta t K(x, y)n(y, t) dy, \quad (4.7)$$

in which $p(x)\Delta t$ is the probability that a block of size x will fracture in a time Δt . In our situation, if Δt is the time interval between fractures, then we need to take $p\Delta t = 1$, and this leads to the difference equation

$$n(x, t + \Delta t) = \int_0^\infty K(x, y)n(y, t) dy, \quad (4.8)$$

and we call this theory *reductive* fragmentation theory, as the block sizes reduce at each step.

We proceed as in section 3.1 to define self-similar fragmentation by means of the self-similar kernel $K(x, y) = \frac{1}{y}g\left(\frac{x}{y}\right)$, and this leads to the reductive equivalent of (3.13),

$$W(\phi, t + \Delta t) = \int_{-\infty}^{\infty} G(\chi)W(\phi - \chi, t) d\chi, \quad (4.9)$$

where G is as defined earlier.

Truncation and advection are determined by choosing a kernel $g(\eta)$ such that $g = 0$ for $\eta > 1 - \Delta\eta$, where we imagine $\Delta\eta$ is small (though this is not necessary). This essentially says that any block fracture yields a following block of maximum relative size $1 - \Delta\eta$, with the details of the grain sizes produced dependent on the kernel g .

We show in the appendix that the solution of (4.9) can then be written as

$$W(\phi, n\Delta t) = U(\phi - \phi_0 - n\Delta\chi, n\Delta t), \quad (4.10)$$

where $\Delta\chi \propto \Delta\eta$, approximately, and $U_n(\xi) \equiv U(\xi, n\Delta t)$ satisfies the difference equation

$$U_{n+1}(\xi) = \int_0^{\infty} G^*(\psi)U_n(\xi - \psi) d\psi, \quad (4.11)$$

and $G^*(\psi)$ is a phase shifted version of G , but satisfies the same integral constraint

$$\int_0^{\infty} G^*(\chi) d\chi = 1, \quad (4.12)$$

and is zero for $\psi < 0$. (4.10) demonstrates the fact that the solution for W is advected downstream in ϕ , at speed $\frac{\Delta\chi}{\Delta t}$.

The solution for U can be written in terms of the Fourier transform. Explicitly,

$$\hat{U}_n = \hat{G}^{*n}. \quad (4.13)$$

As an example, consider the uniform kernel in which g is constant, so that G and therefore $G^* \propto e^{-2A\chi}$. Then $\hat{G}^* = \frac{2A}{2A - ik}$, and thus $\hat{U} = \left(\frac{2A}{2A - ik}\right)^n$, whose inverse is the gamma distribution

$$U_n = \frac{(2A)^n \phi^{n-1}}{\Gamma(n)} e^{-2A\phi}, \quad (4.14)$$

which as we have seen is a reasonable approximation to the coarse part of the distributions. A slightly more general assumption is a power law $g \propto \eta^\lambda$, $\lambda > -1$, indicating a weighting toward production of fines ($\lambda < 0$) or coarse particles ($\lambda > 0$), and this also leads to a gamma function (4.14), but with $2A$ replaced by $A(2 + \lambda)$. Note that the exponent λ is unrelated to its previous use in the Turcotte kernels.

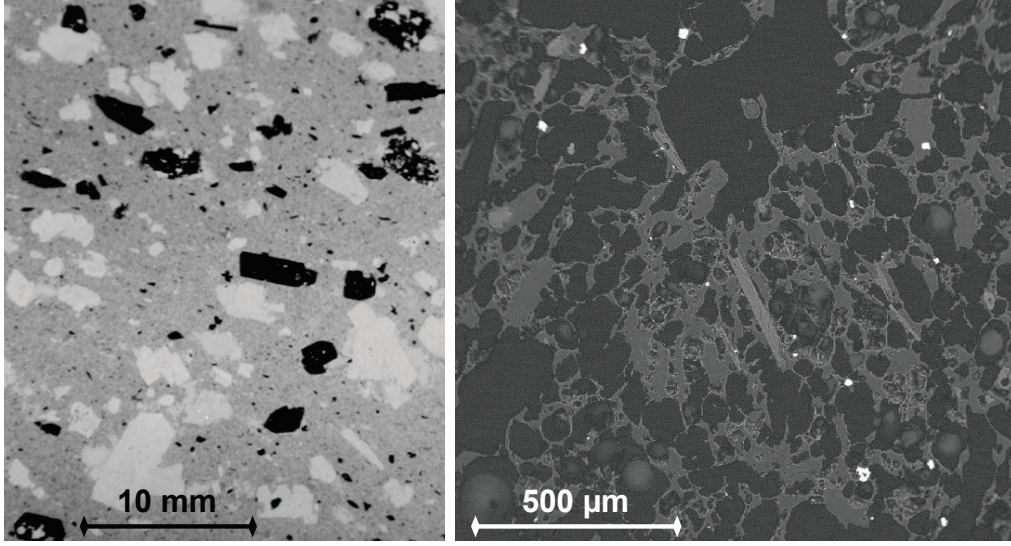


Figure 5: Photographs of Unzen Breadcrustbomb (BKB), used in this study. Left: thin section photograph, showing distribution of vesicles and phenocrysts (mostly dark amphiboles, and white feldspars) in a fine grey groundmass. Right: SEM image of the grey groundmass, showing the microlites (mostly plagioclase) and vesicularity within the groundmass.

4.5 The production of fines

It is clear in figures 1 and 2 that the distributions are heavy-tailed at small particle size (large ϕ). Both figures show that fine particles with $\phi \gtrsim 0$ are produced fairly uniformly as time increases (i.e., initial pressure increases), and the decay at large ϕ is fairly mild. We associate this with the production of fine particles during the fracturing process. Figure 5 shows typical images of the vesicularity of the rock samples. We imagine that as a fracture passes across the sample, a range of particles of sizes $\lesssim 1$ mm ($\phi \gtrsim 0$) is produced, and indeed this is seen in the experimental videos (figure 6).

In order to describe this, we return to the reductive equation (4.8), but now we consider the particle size distribution to consist of a coarse population n_c and a fine population n_f , with the dividing size being x_f . Our assumption is that the fracture of coarse particles produces both coarse and fine particles, but only the coarse particles fracture, essentially because the fine particles are at the scale of the vesicularity, where the fracturing mechanism (exhalation of pore gas) does not apply. We thus take $K = 0$ both for $x > y$ and also for $y < x_f$. In consequence we have

$$n_c(x, t + \Delta t) = \int_{x_f}^{\infty} K(x, y) n_c(y, t) dy, \quad x > x_f, \quad (4.15)$$

and the earlier discussion of the evolving coarse fraction is essentially the same as before, with the same conclusion providing x_f is sufficiently small that it does not

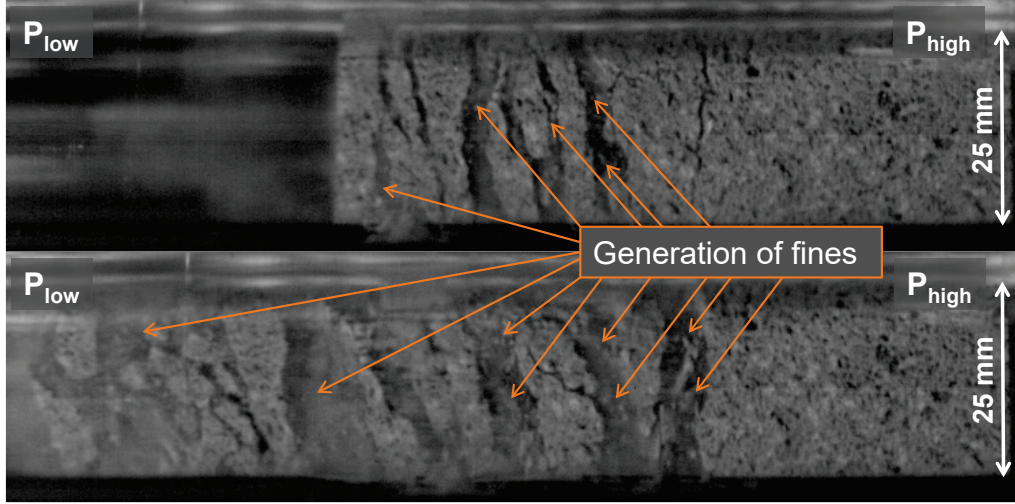


Figure 6: Still frames of a fragmenting rock sample. Both frames are taken from the same ultra-high speed video recorded at 30,000 fps, the time difference between each is 0.7 ms. The sample fragments in a layered fashion following the model proposed by Fowler *et al.* (2010); in between all layers, fine particles of variable size can be identified. Some fines are too small to be resolved as individual particles and appear as ‘dust’. (Note: the sample shown in this figure is different to the one used in this study, but it is very similar in porosity and fragmentation behaviour. This video is part of a study making use of a camera with significantly higher image quality resulting in high quality still frames, which allows detection of fines to be significantly easier than in the videos used in this study.)

affect the coarse fraction. Insofar as we suggest a typical coarse fraction gamma distribution which tends rapidly to zero, this seems reasonable.

The fines fraction is then given by

$$n_f(x, t + \Delta t) = \int_{x_f}^{\infty} K(x, y) n_c(y, t) dy, \quad x < x_f, \quad (4.16)$$

and depends on the choice of the fragmentation kernel K when $x < x_f$, which represents the production of fine $x < x_f$ from coarse $y > x_f$. In keeping with our earlier discussion, we wish to retain the power law of the Brown kernel, but this needs to be modified so that $K \rightarrow 0$ as $x \rightarrow x_f -$. The simplest choice with this behaviour is the modified Brown kernel

$$K = K_f = C x^{\nu-1} \left\{ \ln \left(\frac{x_f}{x} \right) \right\}^{\mu}, \quad x < x_f, \quad (4.17)$$

where volume conservation requires $\nu > -1$, and we have introduced the logarithmic factor so that $K_f = 0$ at $x = x_f$, assuming as we do that $\mu > 0$. As for the Brown kernel, the exponent ν as well as μ will be assessed by comparison with the experimental data, but the pre-factor is determined by a mass conservation argument.

This is detailed in the appendix, where it is shown that we can write (4.17) in the form

$$K_f = B^* \left(\frac{y}{x_f} \right)^{2/3} \frac{x_f^{\nu-1}}{x_f^\nu} \left\{ \ln \left(\frac{x_f}{x} \right) \right\}^\mu, \quad (4.18)$$

where B^* is an $O(1)$ number which depends on the precise amount of fines produced in the fracturing process.

Note that this fines production kernel is *not* self-similar. Putting (4.18) into (4.16), we obtain

$$n_f(x, t + \Delta t) = \frac{B^* x_f^{\nu-1}}{x_f^{\nu+2/3}} \left\{ \ln \left(\frac{x_f}{x} \right) \right\}^\mu \int_{x_f}^{\infty} y^{2/3} n_c(y, t) dy. \quad (4.19)$$

Translating this to $W(\phi, t)$, we have, with an obvious notation,

$$W^f(\phi, t + \Delta t) = A^{1+\mu} B^* e^{-\frac{1}{3}A\phi_f} (\phi - \phi_f)^\mu e^{-(\nu+1)A(\phi-\phi_f)} \int_{-\infty}^{\phi_f} e^{\frac{1}{3}A\psi} W(\psi, t) d\psi, \quad (4.20)$$

when $\phi > \phi_f$. If we assume that $\phi_f - \phi_0$ is large, and that W_n is given by the gamma distribution in (4.14), then (4.20) simplifies at time step $n > 0$ to

$$W_n^f = A^{1+\mu} B^* e^{-\frac{1}{3}A\phi_f} \left(\frac{6}{5} \right)^n (\phi - \phi_f)^\mu e^{-(\nu+1)A(\phi-\phi_f)}, \quad (4.21)$$

which is another gamma distribution, but one which grows in time without advection. This description matches the principal features of the tails of the distributions in figure 2, which are that they increase regularly with initial pressure p_0 (thus t and thus n), and that they decay weakly with ϕ . Indeed, comparison with (A.7) indicates that $\nu = -\frac{1}{3}D$, where D is fractal dimension, as described in the appendix. Typical observed values of D are in excess of 1.8 (Hartmann 1969, Turcotte 1997, p. 44), so that $\nu < -0.6$, which would suggest that $(\nu + 1)A < 0.8$, which seems consistent with the slow decay in figure 2. In principle, the value of ν should depend on the distribution of vesicle spacing, as seen in figure 5. Hartmann notes that the lower range of D is associated with ‘simple fragmentation’ with little abrasion, as may be appropriate here. It should be pointed out his value for ‘ash and pumice’ is $D = 3.54$, and commonly $D > 3$ for such deposits, but he associates such high values with extreme grinding and abrasion, which is less applicable here. It is an interesting question how such exponents are obtained, but not one of relevance here. Note that (A.7) requires that $D < 3$ for sufficiently large ϕ , so that values $D > 3$ must represent the rising limb of the distribution; it is natural to suppose that the falling limb is lost as the airborne ash cloud.

In summary, we have used assumed power-law type kernels to produce predicted forms of GSD for experiments with different initial confining pressures. These pressures serve as proxy measurements of fragmentation time, as explained in section 4.1. We have shown qualitatively that the theory has the possibility of explaining the data, but we have as yet no quantitative comparison. This will be done in the following section, where we will choose values for the wealth of parameters which are consistent with the data.

p	\tilde{A}	α	ϕ^*	a^*	n
2.5	200	5	-4	0.8	3
5	100	2	-4	0.8	3
6	95	1.82	-3.7	0.8	3
10	70	1.67	-3.5	0.8	3

Table 1: Values of the fitting parameters using (5.2) corresponding to the approximations in figure 4.

5 Discussion

We define the gamma distribution function as

$$\mathcal{G}(x, a, \nu) = \frac{a^\nu x^{\nu-1} e^{-ax}}{\Gamma(\nu)} \quad (5.1)$$

if $x > 0$, and $\mathcal{G} = 0$ for $x < 0$. Note that its integral is one. The fitting curve in figure 4 is thus $V = 100 \mathcal{G}(\Phi, 0.8, 3)$, and the specific approximations there for $W(\phi, p)$ (measured as weight percent) are thus of the form

$$W(\phi, p) \approx \tilde{A} \mathcal{G}[\alpha(\phi - \phi^*), a^*, n], \quad (5.2)$$

where the values of p , \tilde{A} , α , ϕ^* , a^* and n corresponding to the fitting approximations in figure 4 are given in table 1. Noting that

$$\mathcal{G}(\alpha x, a, \nu) = \frac{1}{\alpha} \mathcal{G}(x, \alpha a, \nu), \quad (5.3)$$

(5.2) can also be written in the form

$$W(\phi, p) \approx \frac{\tilde{A}}{\alpha} \mathcal{G}[\phi - \phi^*, \alpha a^*, n]. \quad (5.4)$$

We now wish to relate these fitted curves to the predictions given by (4.10) and (4.14) for the coarse fraction, and to then adjust the prediction by including the fine fraction prediction (4.21). Equations (4.10) and (4.14) suggest a coarse approximation

$$W \approx A^* \mathcal{G}[\phi - \phi^*, \alpha a^*, n], \quad (5.5)$$

where

$$\phi^* = \phi_0 + n \Delta \chi, \quad (5.6)$$

n representing time is a proxy for initial confining pressure p , and in (4.14) we would have $\alpha a^* = 2A$, or for the more general power law $g \propto \eta^\lambda$ (see after (4.14)), $\alpha a^* = A(2 + \lambda)$, thus $\lambda < 0$ would indicate a weighting towards fines production if $\alpha a^* \lesssim 4$. The value of A^* should be 50, since the sum of the weight fractions $\sum_i W_i = 100\%$, while the integral $\int_{-\infty}^{\infty} W d\phi \approx \sum_i W_i \Delta\phi = 50$, since the bin widths of the data are

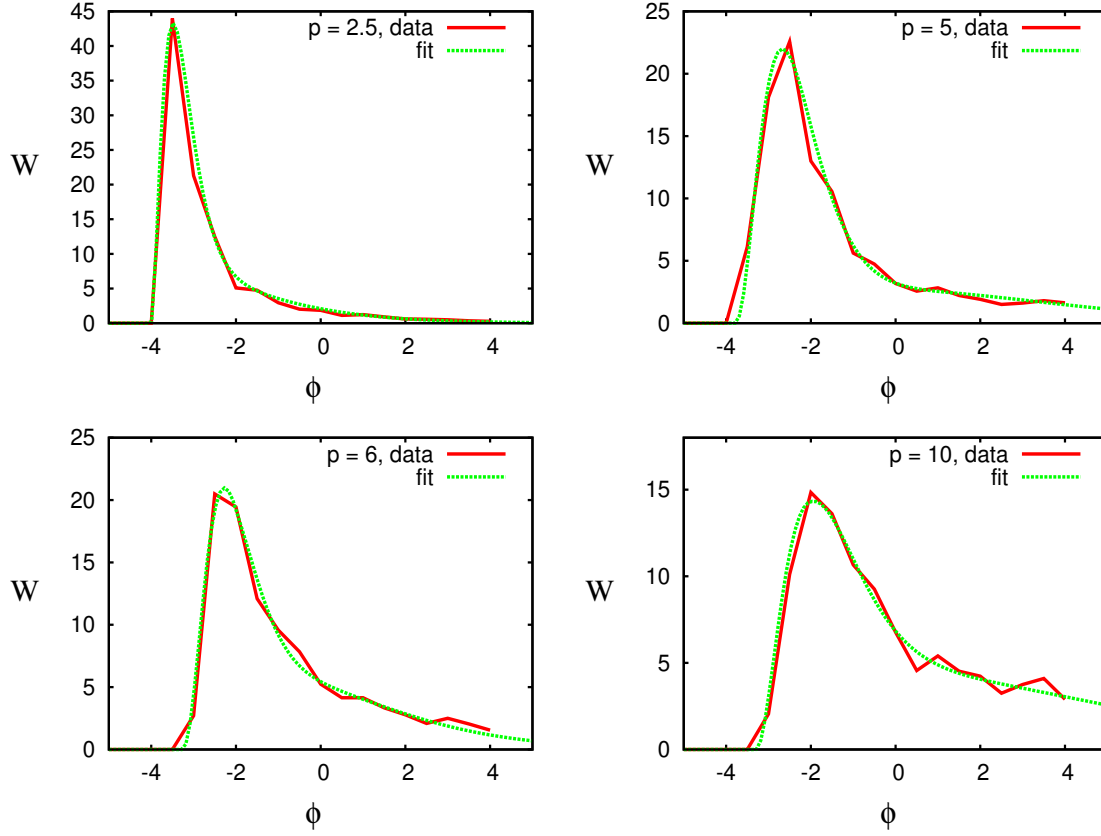


Figure 7: Data (red (online) curves) and fitted curves (green online) from the approximating formula in (5.10).

$\Delta\phi = 0.5$. Since the integral of g is one, this implies $A^* = 50$. Bearing in mind (5.3), (5.5) is equivalent for any α to

$$W \approx A^* \alpha \mathcal{G}[\alpha(\phi - \phi^*), a^*, n], \quad (5.7)$$

which is of the form (5.2), with $\tilde{A} = A^* \alpha$.

We now add the fines production formula (4.21). This can be written in the form

$$W_n^f = C^* \beta^n \mathcal{G}(\phi - \phi_f, \gamma, 1 + \mu), \quad (5.8)$$

where

$$\gamma = (1 + \nu)A, \quad C^* = \frac{3B}{2} e^{-\frac{1}{3}A\phi_f}, \quad \beta = 1.2, \quad (5.9)$$

and $B < 1$ is a number associated with the fracturing process, defined in the appendix before (A.12).

We add the fines fraction to the coarse fraction, subtracting a corresponding part of the coarse distribution to conserve mass. Writing $b = C^* \beta^n$, this suggests a combined approximation

$$W_n = A^* [(1 - b) \alpha \mathcal{G}(\alpha(\phi - \phi^*), a^*, n) + b \mathcal{G}(\phi - \phi_f, \gamma, 1 + \mu)]. \quad (5.10)$$

p	A^*	$b \propto \beta^n$	α	$n\Delta\chi$	a^*	n	ϕ_f	γ	μ	$\nu = \frac{\gamma}{A} - 1$	$\lambda = \frac{\alpha a^*}{A} - 2$
2.5	56	0.36	5	1	0.8	3	-4	0.8	1	-0.62	-0.08
5	55.1	0.28	2	1.2	1.15	3.6	-2	0.5	1.5	-0.76	-0.89
6	51.7	0.38	1.82	1.7	1.6	4	-2	0.75	1.5	-0.64	-0.6
10	62.9	0.47	1.67	1.7	1	3.2	-2	0.4	1.5	-0.81	-1.20

Table 2: Values of the parameters in (5.10) corresponding to the approximations in figure 7. The values of $n\Delta\chi$ are determined from (5.6), assuming $\phi_0 = -5$. Note that $\alpha a^* < 2A$, as discussed following (5.6).

We have used this formula to fit the data, and the results are shown in figure 7. In fitting the data, we used initially the values in table 1 with some adjustment to fit the coarse part, and then the parameters of the fine part were adjusted (principally the decay parameter γ and the amplitude parameter b) to fit the heavy tail. The fits are obviously very good, though we have not endeavoured either to find the best fit or to choose parameters which best suit our suggestion that the data represents increasing values of n , although it can be seen from table 2 (columns for b , $n\Delta\chi$ and n) that this is largely the case. We think it more significant that the analytic form of the prediction can be made to fit the data relatively easily; as anyone will know who has tried, this is not always the case.

One comment on the parameters is the value of A^* , which ought to be 50. This is approximately the case, although the value for $p = 10$ is a bit high. This is due to the fact that while our fitted curve has a component with non-zero area in $\phi > 4$, the data is truncated by the finest mesh size at $\phi = 4$; thus the final bin of the data includes all the fines with $\phi > 4$, although the fact that the final bin has a quantity commensurate with the trend of the other bins actually suggests that there is a cut-off size in the fine particle production; this might explain why the fitted curves do so well up to $\phi = 4$.

A second comment concerns the choice of γ given in (5.9). As indicated in the appendix by (A.7), the corresponding fractal dimension is

$$D = 3 \left(1 - \frac{\gamma}{A} \right), \quad (5.11)$$

and evidently we expect $\gamma < A \approx 2.08$. This it is, and the fitted range 0.4–0.8 corresponds to a value of $D = 1.85$ – 2.42 . These are well within the range quoted by Turcotte (1986, table 1).

6 Conclusions

Grain size distributions from experiments on the fragmentation of volcanic rocks have a characteristic shape which depends on the initial confining pressure, and which can

be well represented by the sum of two gamma distributions. We suggest that the variation with confining pressure represents an equivalent evolution of the distribution with time following pressure release, based on our earlier theory (Fowler *et al.* 2010), and we then pose a stochastic process theory to describe the evolution of the distribution with time. This theory introduces the concept of self-similar fragmentation kernels, and leads to a predicted gamma distribution for coarse fragments assuming a general power law kernel. We further associate the heavy tail of the distributions with a secondary process, whereby the primary fracturing produces fine particles. A generalised power law for this (non-similar) process predicts a second gamma distribution whose amplitude grows geometrically in time. We then show that the combined distributions can easily fit the observations, and that the fitting parameters are broadly consistent with the hypothesis that the data represents an effective time evolution of the grain size distribution.

Data accessibility

The data plotted in figures 1 and 2 is contained in the electronic supplementary material.

Competing interests

We have no competing interests.

Authors contributions

B.S. performed the experiments and found the grain-size distribution, and produced the experimental figures. A.C.F. devised and solved the model, and wrote the paper. Both authors worked on the final submitted text.

Acknowledgements

We have no acknowledgements.

Funding statement

A.C.F. acknowledges the support of the Mathematics Applications Consortium for Science and Industry (www.macsi.ul.ie) funded by the Science Foundation Ireland grant 12/1A/1683. B.S. acknowledges the support of the European Commission (FP7-MC-ITN, grant number 289976: NEMOH).

Ethics statement

This research poses no ethical considerations.

Appendix

We relate the number density n to the volume or weight fraction density W measured in terms of ϕ , as discussed in section 3.1. $nx dx$ is the volume of fragments in the range $(x, x + dx)$, and so we have

$$\frac{nx dx}{x_0} = -W d\phi \quad (\text{A.1})$$

(the minus sign because ϕ increases with decreasing x), and it follows that

$$W = \frac{Anx^2}{x_0}. \quad (\text{A.2})$$

In addition we define

$$p(x) = P(\phi), \quad G(\chi) = Ae^{-2A\chi}g(e^{-A\chi}); \quad (\text{A.3})$$

note that $G = 0$ for $\chi < 0$. Then the master equation (3.2) takes the form

$$W_t = \int_{-\infty}^{\infty} G(\psi)P(\phi - \psi)W(\phi - \psi, t) d\psi - P(\phi)W. \quad (\text{A.4})$$

The form (3.13) follows from the choice $P = 1$.

Fractal dimension

Another commonly measured quantity is the number of fragments of radius larger than R , and we will denote this as $M(R)$. We have

$$M(R) = \int_{V(R)}^{x_0} n dx, \quad V(R) = \frac{4}{3}\pi R^3, \quad (\text{A.5})$$

and in terms of W , this is

$$M(R) = \int_{\phi_0}^{\frac{1}{A} \ln\{x_1/V(R)\}} e^{A(\phi - \phi_0)} W d\phi. \quad (\text{A.6})$$

The fractal dimension D of a power law distribution is given by the relation $M \sim R^{-D}$ for small R (Turcotte 1997), and in terms of W , this implies

$$W \sim \exp\{A(\frac{1}{3}D - 1)\phi\} \text{ if } M \sim R^{-D} \quad (\text{A.7})$$

at large ϕ . Convergence at large ϕ requires $D < 3$, as is commonly found (Turcotte 1997).

Reductive fragmentation theory

We consider the equation (4.9) for W :

$$W(\phi, t + \Delta t) = \int_{-\infty}^{\infty} G(\chi) W(\phi - \chi, t) d\chi, \quad (\text{A.8})$$

but now we suppose

$$G = 0 \quad \text{for} \quad \chi < \Delta\chi \equiv \frac{1}{A} \ln \left(\frac{1}{1 - \Delta\eta} \right). \quad (\text{A.9})$$

Approximately, $\Delta\chi \approx \frac{\Delta\eta}{A}$. We define

$$G^*(\chi) = G(\Delta\chi + \chi), \quad (\text{A.10})$$

and then (A.8) can be written as

$$W(\phi, t + \Delta t) = \int_0^{\infty} G^*(\psi) W(\phi - \Delta\chi - \psi, t) d\psi, \quad (\text{A.11})$$

where $G^*(\psi)$ satisfies the integral constraint (4.12), and is zero for $\psi < 0$. The solution of (A.11) then proceeds as in the main text.

Fines production

We consider the value of the pre-factor C in (4.17). The volume of fines produced from a fracture of a block of size y is $\int_0^{x_f} x K(x, y) dx$, and assuming the volume produced from a circular fracture of diameter d is $\frac{1}{4} B \pi d^2 d_f$, where $y = \frac{1}{6} \pi d^3$, $x_f = \frac{1}{6} \pi d_f^3$ and $B < 1$, equating the two implies

$$C = \frac{\pi B (\nu + 1)^{1+\mu} d_f d^2}{4 x_f^{\nu+1} \Gamma(\mu + 1)}, \quad (\text{A.12})$$

which gives (4.18), where

$$B^* = \frac{3B(\nu + 1)^{1+\mu}}{2\Gamma(\mu + 1)}. \quad (\text{A.13})$$

References

- Alatorre-Ibargüengoitia, M. A., B. Scheu and D. B. Dingwell 2011 Influence of the fragmentation process on the dynamics of Vulcanian eruptions: an experimental approach. *Earth Planet. Sci. Letts.* **302** (1-2), 51–59.
- Alidibirov, M. and D. B. Dingwell 1996 Magma fragmentation by rapid decompression. *Nature* **380**, 146–148.

- Bonadonna, C. and B.F. Houghton 2005 Total grain-size distribution and volume of tephra-fall deposits. *Bull. Volcanol.* **67**, 441–456.
- Brown, W.K. 1989 A theory of sequential fragmentation and its astronomical applications. *J. Astrophys. Astr.* **10**, 89–112.
- Brown, W.K. and K.H. Wohletz 1995 Derivation of the Weibull distribution based on physical principles and its connection to the Rosin–Rammler and lognormal distributions. *J. Appl. Phys.* **78** (4), 2,758–2,763.
- Cas, R. A. F. and J. V. Wright 1987 *Volcanic successions: modern and ancient*. Chapman and Hall, London.
- Cheng, Z. and S. Redner 1990 Kinetics of fragmentation. *J. Phys. A Math. Gen.* **23**, 1,233–1,258.
- Dufek, J., M. Manga and A. Patel 2012 Granular disruption during explosive volcanic eruptions. *Nature Geosci.* **5**, 561–564.
- Elek, P. and S. Jaramaz 2008 Fragment size distribution in dynamic fragmentation: geometric probability approach. *FME Trans.* **36**, 59–65.
- Fowler, A. C., B. Scheu, W. T. Lee and M. J. McGuinness 2010 A theoretical model of the explosive fragmentation of vesicular magma. *Proc. R. Soc. A* **466**, 731–752.
- Girault, F., G. Carazzo, S. Tait, F. Ferruccio and E. Kaminski 2014 The effect of total grain-size distribution on the dynamics of turbulent volcanic plumes. *Earth Planet. Sci. Letts.* **394**, 124–134.
- Hartmann, W.K. 1969 Terrestrial, lunar, and interplanetary rock fragmentation. *Icarus* **10**, 201–213.
- Ichihara, M., D. Rittel, and B. Sturtevant 2002 Fragmentation of a porous viscoelastic material: implication to magma fragmentation., *J. Geophys. Res.* **106**, 2,226–2,239.
- Kaminski, E. and C. Jaupart 1998 The size distribution of pyroclasts and the fragmentation sequence in explosive volcanic eruptions. *J. Geophys. Res.* **103** (B12), 29,759–29,779.
- Kolmogorov, A. N. 1941 Über das logarithmisch normale Verteilungsgesetz der Dimensionen der Teilchen bei Zerstückelung. *Dokl. Akad. Nauk. SSSR* **31**, 99–101. Translated as “The logarithmically normal law of distribution of dimensions of particles when broken into small parts”, NASA technical translation NASA TT F-12,287, NASA, Washington, D. C., June 1969.
- Kremers S., B. Scheu, B. Cordonnier, O. Spieler and D.B. Dingwell 2010 Influence of decompression rate on fragmentation processes: an experimental study. *J. Volcanol. Geotherm. Res.* **193** (3-4), 182–188.

- Kueppers, U., B. Scheu, O. Spieler and D. B. Dingwell 2006 Fragmentation efficiency of explosive volcanic eruptions: a study of experimentally generated pyroclasts. *J. Volcanol. Geotherm. Res.* **153** (1-2), 125-135.
- Mackaman-Lofland, C, B. D. Brand, J. Taddeucci and K. Wohletz 2014 Sequential fragmentation/transport theory, pyroclast size-density relationships, and the emplacement dynamics of pyroclastic density currents—a case study on the Mt. St. Helens (USA) 1980 eruption. *J. Volcanol. Geotherm. Res.* **275**, 1–13.
- Mader, H. M., Y. Zhang, J. C. Phillips, R. S. J. Sparks, B. Sturtevant, and E. Stolper 1994 Experimental simulations of explosive degassing of magma. *Nature* **372**, 85–88.
- Müller S., B. Scheu, O. Spieler and D.B. Dingwell 2008 Permeability control on magma fragmentation. *Geology*, **36** (5), 339–402.
- Namiki, A. and M. Manga 2008 Transition between fragmentation and permeable out-gassing of low viscosity magmas. *J. Volcanol. Geotherm. Res.* **169**, 48–60.
- Perfect, E. 1997 Fractal models for the fragmentation of soils and rocks: a review. *Engng. Geol.* **48**, 185–198.
- Perugini, D. and U. Kueppers 2012 Fractal analysis of experimentally generated pyroclasts: a tool for volcanic hazard assessment. *Acta Geophysica* **60** (3), 682-698.
- Phillips, J. C., S. J. Lane, A.-M. Lejeune and M. Hilton 1995 Gum-rosin-acetone system as an analogue to the degassing behaviour of hydrated magmas. *Bull. Volcanol.* **57**, 263–268.
- Rager, A. H., E. I. Smith, B. Scheu and D. B. Dingwell 2014 The effects of water vaporization on rock fragmentation during rapid decompression: implications for the formation of fluidized ejecta on Mars. *Earth Planet. Sci. Letts.* **385**, 68–78.
- Rieu, M. and E. Perrier 1998 Fractal models of fragmented and aggregated soils. In: *Fractals in soil science*, eds. P. Baveye, J.-Y. Parlange and B. A. Stewart, CRC Press, Boca Raton, pp. 169–202.
- Richard D., B. Scheu, S. P. Mueller, O. Spieler and D. B. Dingwell 2013 Outgassing: influence on speed of magma fragmentation. *J. Geophys. Res. Solid Earth* **118**, doi:10.1002/jgrb.50080.
- Scheu, B., O. Spieler and D. B. Dingwell 2006 Dynamics of explosive volcanism at Unzen volcano: an experimental contribution. *Bull. Volcanol.* **69**, 175–187.
- Scheu, B., U. Kueppers, S. Mueller, O. Spieler and D. B. Dingwell 2008 Experimental volcanology on eruptive products of Unzen volcano. *J. Volcanol. Geotherm. Res.* **175**, 110–119.

- Spieler, O., B. Kennedy, U. Kueppers, D.B. Dingwell, B. Scheu and J. Taddeucci
2004 A fragmentation threshold for the initiation and cessation of explosive
eruptions. *Earth Planet. Sci. Letts.* **226** (1-2), 139–148.
- Turcotte, D.L. 1986 Fractals and fragmentation. *J. Geophys. Res.* **91** (B2), 1,921–
1,926.
- Turcotte, D.L. 1997 Fractals and chaos in geology and geophysics, 2nd edition.
C. U. P., Cambridge.
- Villerraux, E. 2007 Fragmentation. *Ann. Revs. Fluid Mech.* **39**, 419–446.
- Wohletz, K.H., M.F. Sheridan and W.K. Brown 1989 Particle size distributions
and the sequential fragmentation/transport theory applied to volcanic ash. *J.*
Geophys. Res. **94** (B11), 15,703–15,721.